Science Advances

AAAS

advances.sciencemag.org/cgi/content/full/4/5/eaar5492/DC1

Supplementary Materials for

Orientation-independent room temperature optical ^{13}C hyperpolarization in powdered diamond

Ashok Ajoy, Kristina Liu, Raffi Nazaryan, Xudong Lv, Pablo R. Zangara, Benjamin Safvati, Guoqing Wang, Daniel Arnold, Grace Li, Arthur Lin, Priyanka Raghavan, Emanuel Druga, Siddharth Dhomkar, Daniela Pagliero, Jeffrey A. Reimer, Dieter Suter, Carlos A. Meriles, Alexander Pines

Published 18 May 2018, *Sci. Adv.* **4**, eaar5492 (2018)
DOI: 10.1126/sciadv.aar5492

This PDF file includes:

CONTENTS

I. METHODS AND MATERIALS

A. Surface area gains due to diamond powder

As presented in the main paper, the experiments in this work were performed with $200 - 250\mu$m diamond micro-particles from Element6 (Fig. 5C), with ≈1ppm NV center concentration. The average edge length was found to be 87 ± 3.9 μm and this measurement was used for all further calculations of surface area and volume.

Diamond powder has a surface area per unit volume orders of magnitude larger than a single crystal of equivalent mass, even considering special surface patterning [36].The surface area of the particles was calculated using $A = (6 + 12\sqrt{3})a^2$ where a is the edge length. The average particle surface area was calculated to be 0.203 ± 0.0004 mm^2. Volume was calculated using the formula $V = 8\sqrt{2}a^3$, yielding an average volume of $(7.45 \pm 0.00067) \times 10^{-3}$ mm^3 and providing a surface area to volume ratio of 27.1 mm^{-1}.

The mass of the entire sample of particles used in Fig. 2A of the main paper was 7.50 ± 0.25 mg. Using the known density of diamond (3.51 mg/mm^3), the total volume of sample was calculated to be 2.14 ± 0.07 mm^3. Dividing by the individual particle volume, the number of diamond particles was found to be 287 ± 27 diamonds, giving a total surface area of 58.3 ± 5.1 mm^2, equivalent to 7.77 ± 0.72 mm^2/mg. When compared to a diamond crystal of same mass and with dimensions 1mm×1mm square base and 2.09 mm height, assuming only the 1 mm by 1 mm base makes contact with the liquid, the arrangement of many small particles results in a 58.3-fold increase in surface area of 7.77 mm^2/mg. In the case of diamond nanoparticles, with 100 nm edge lengths and a total volume of 2.14 mm^3 and surface area of 6744 mm^2/mg, the increase in surface area would be more than 6700-fold. This dramatic increase in surface area would be highly beneficial in transferring spin polarization from diamond to a liquid sample. One method of lithographic application of nanogratings with 400 nm pitch with a depth of up to 3 micron increases the surface area of 2 mm x 2 mm x 0.5 mm diamond chips by 15, giving a surface area to mass ratio of 8.55 mm^2/mg [36]. Even with extensive processing, the resulting surface area is much less than that possible with 100 nm particles.

Our orientation independent technique can be used to hyperpolarize nano- and micro-particles of diamonds, both dry as well as suspended in solution (see Supplementary Material Sec. I B). We have been able to polarize particles of sizes 1, 25, 200 and 400μm, and have found that the exact amount of polarization depends on optical penetration depth, concentration of P1 centers, and quality of sample preparation that sets the low field T_1. We measured the T_1 times of the $200 - 250\mu$m particles to be 395.7s at $\mathbf{B}_0 = 7$T and 10.19s at $\mathbf{B}_{\text{pol}} = 8$mT. Since the DNP polarization is inhomogeneous, i.e. spins closer to the NV centers are more strongly polarized, spin diffusion between them also causes a signal decay at low fields, leading to a super-exponential fall in signal. This feature slightly underestimates the T_1 at $\mathbf{B}_{\text{pol}}$. A more detailed analysis of the spin diffusion factors affecting the T_1 will be presented elsewhere.

B. DNP of particles in solution

While in the paper we focus on *dry* particles in the sample tube, fig. S1 demonstrates the case when DNP is performed with the particles immersed in different solvents under the same conditions. The solvent, with no air bubbles, is held under slight pressure by the plunger (fig. S6A inset). We find that the DNP enhancements are boosted by a factor ≈ 2, which we attribute potentially to better optical penetration into the diamonds due to better refractive index matching (fig. S1B). We note that DNP performs without any visible sample heating inspite of microwave irradiation near ≈ 2.45GHz, which is the operating frequency for conventional microwave ovens. This is likely due to water having low permittivity at that frequency [37].

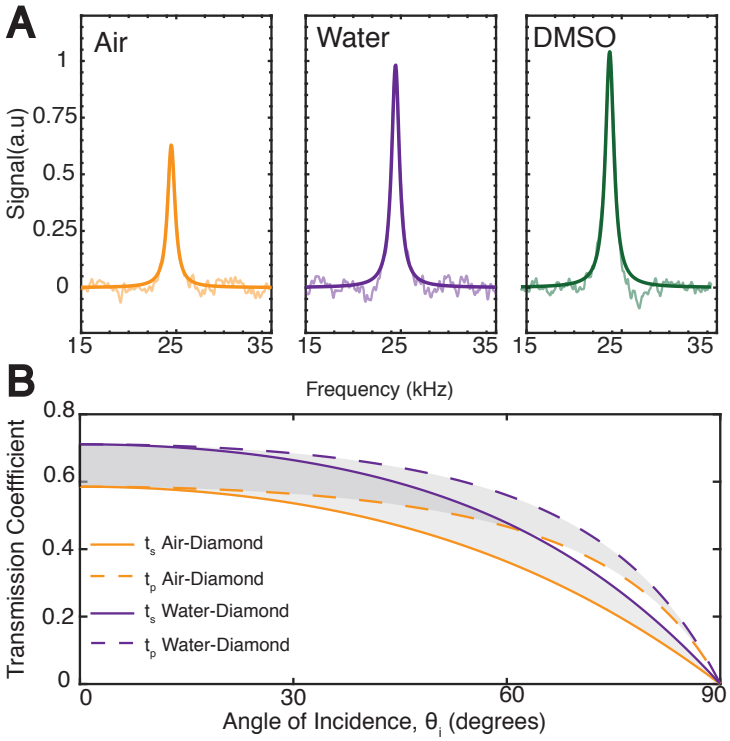

Figure S1. Enhanced ^{13}C DNP for particles in solution. (A) Panels indicate that ^{13}C polarization enhancements are in fact enhanced when the particles are immersed in solvents, which we attribute to better refractive index matching to diamond. We compare the obtained enhancements for e6 200μm diamond microparticles (Fig. 5C of main paper) dry ($n_r = 1$), in water ($n_r = 1.33$), and in DMSO ($n_r = 1.48$). (B) The effect of better index matching obtained through Fresnel equations that relate the transmission coefficients between air-diamond and water-diamond interfaces. Here *s*- and *p*- refer to different polarizations, and for random diamond powder both contribute.

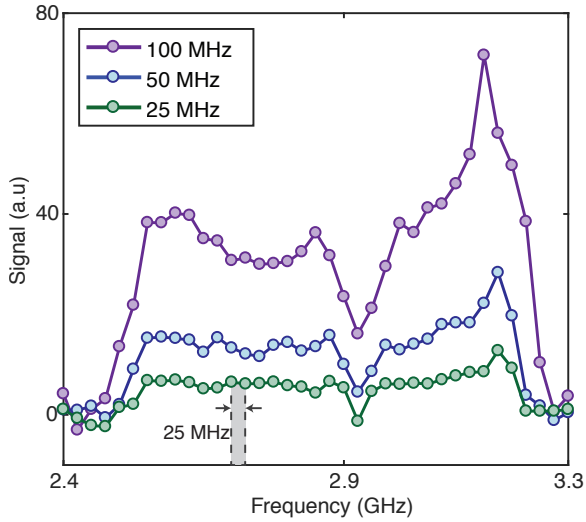

Figure S2. Electron powder pattern measured via ^{13}C DNP. Panel illustrates the obtained NV center powder pattern indirectly obtained by microwave sweeps of varying widths (in legend) according to Fig. 1B and measuring the ^{13}C signal. The obtained signal is a convolution of the underlying powder pattern with the sweep width. We find the same sign of the ^{13}C hyperpolarization over the entire sweep, and remarkably that even rather large sweep widths eg. 100MHz can provide an faithful representation of the powder pattern.

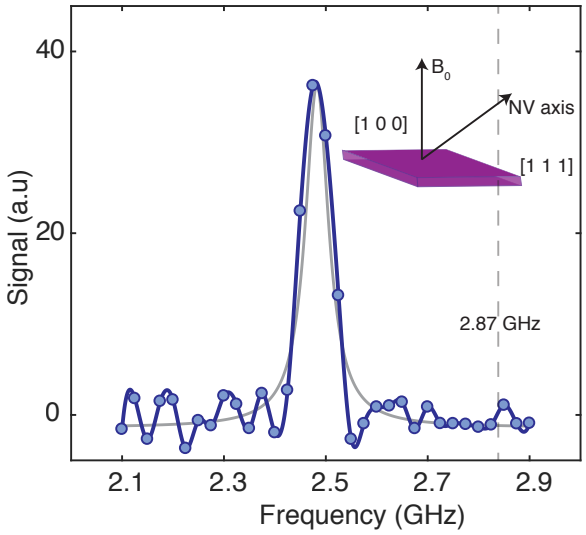

Figure S3. **Single crystal electronic lineshape measured via ^{13}C DNP.** Panel illustrates that by performing ^{13}C DNP in a 25MHz window on a macroscopic single crystal (0.311 x 3.239 x 3.238 mm) sweeping from 2.4 to 2.7 GHz it is possible to map the underlying NV center electronic lineshape. In this case the magnetic field $\mathbf{B}_{\text{pol}} \approx 24.6$mT is aligned at the magic angle 54.7° to the NV axis (inset) leading to the single spectral line for all four families of NV center orientations. Note that in these experiments the ^{13}C spins indirectly report the electronic spectrum as opposed to direct ODMR measurements.

II. INDIRECT NV SPECTROSCOPY BY ^{13}C DNP

In the experiments in Fig. 3 of the main paper, we performed spectroscopy of the inhomogenously broadened NV center lineshape corresponding to the different NV orientations ("*powder pattern*") indirectly. This was done by measuring the ^{13}C enhancement sweeping microwaves through multiple 100MHz bandwidths, each bandwidth producing one data point. The relative signal obtained compared across multiple 100MHz windows reflects the powder pattern and is its convolution with the sweep bandwidth.

For clarity, and to quantify the effect of this convolution, in fig. S2 we repeat the experiment by varying the size of the sweep bandwidth at low field. The smallest window (25MHz) approaches the intrinsic linewidth of an individual NV center ($\approx$ 10MHz). As expected the absolute value of the signal drops for smaller sweep windows, but the shape of the pattern remains qualitatively identical in each case. This proves convenient experimentally, because a quick map of the powder pattern allows one to optimize the full sweep bandwidth for maximum ^{13}C polarization without ODMR or related optical spectroscopy.

Fig. S3 illustrates this also for a single crystal, where the ^{13}C DNP is used to report on the underlying NV center spectral lineshape without ODMR. The experiment also demonstrates that our DNP mechanism is as effective on single crystals, and orientation independent (all four possible NV directions form a 54.7° angle with B_0 in fig. S3).

III. MECHANISM FOR ORIENTATION INDEPENDENT POLARIZATION TRANSFER

In this section, we outline the low-field DNP mechanism that governs the polarization transfer in our experiments. Before delving into the formal details, let us briefly summarize one more time its experimentally determined characteristics.

(i) The mechanism works predominantly at low field, 1-30mT.

The exact field dependence has not been studied, however we measure no DNP enhancement beyond 100mT.

(ii) The mechanism provides polarization transfer independent of the orientation of the NV center relative to the field direction, and subsequently allows the hyperpolarization of diamond powder (see Fig. 4 of main paper, and fig. S2).

(iii) The sign of the ^{13}C hyperpolarization depends only on the direction of microwave sweep (see Fig. 2C).

(iv) A low-to-high frequency sweep gives the nuclear spin polarized along the field (i.e. the same sign as thermal Boltzmann polarization).

(v) Sweeping microwaves in the $m_s = -1$ or $m_s = +1$ NV manifold makes no difference to the obtained ^{13}C hyperpolarization sign (Fig. 4A), which instead only depends on the MW sweep direction.

(vi) Even a $\lesssim$25MHz sweep window is enough to hyperpolarize spins (see fig. S2). We expect the ultimate sweep window where hyperpolarization is achievable to be even smaller, but this was not experimentally verified due to lower absolute signal with decreasing window size. This points to the fact that the DNP mechanism does not rely only on closest shell ^{13}C nuclei.

(vii) We experimentally find an optimal MW sweep rate of 40MHz/ms at a 24mT polarizing field (Fig. 2D).

(viii) This optimal MW sweep rate is independent of laser power (fig. S8).

(ix) The obtained enhancements are found to decrease with high laser power beyond a certain threshold $\approx$2.5mW/mm^2 for 532nm excitation. Note that this number is also a function of the optical penetration depth in the sample, and potentially complex dynamics between the NV charge states [38].

(x) There is an optimal MW power (Rabi frequency), and increasing power leads to a drop in polarization transfer efficiency (Fig. 2D inset).

To model the observed spin dynamics, we use a two-spin system formed by the NV electronic spin and a hyperfine-coupled carbon, which is valid in the limit of a dilute ^{13}C concentration (1% in the present case, the natural ^{13}C abundance). The governing lab frame Hamiltonian is given by

$$\begin{aligned}\mathcal{H} = \Delta S_z^2 - \gamma_e \vec{B}\cdot\vec{S} - \gamma_C \vec{B}\cdot\vec{I} + A_{zz}S_zI_z \\ + A_{yy}S_yI_y + A_{xx}S_xI_x + A_{xz}S_xI_z + A_{zx}S_zI_x\end{aligned} \quad (1)$$

where $\vec{S} \equiv (S_x, S_y, S_z)$ and $\vec{I} \equiv (I_x, I_y, I_z)$ respectively denote the NV and ^{13}C vector spin operators, γ_e (γ_C) is the NV (^{13}C) gyromagnetic ratio, $A_{\alpha\beta}$ with $\alpha, \beta = x, y, z$ are the components of the hyperfine tensor, and $\vec{B} \equiv (\sin\vartheta\ \cos\varphi, sin\vartheta\ \sin\varphi, cos\vartheta)$ is the magnetic field (10-30 mT) oriented along an axis characterized by a polar (azimuthal) angle ϑ (φ) in a reference frame whose z-axis coincides with the NV direction; without loss of generality, we assume the ^{13}C nucleus is contained within the xz-plane. Within the $m_S = \pm 1$ states, the hyperfine coupling produces a ^{13}C splitting

$$\omega_C^{(\pm 1)} = \sqrt{(A_{zz} \mp \gamma_C B\cos\vartheta)^2 + A_{zx}^2} \quad (2)$$

For the $m_S = 0$ manifold, second-order perturbation theory leads to the approximate formula

$$\begin{aligned}\omega_C^{(0)} \approx \gamma_C B \\ + 2\Big(\frac{\gamma_e B}{\Delta}\Big)\sin\vartheta\big(\sqrt{A_{xx}^2 + A_{zx}^2}\cos^2\varphi + A_{yy}\sin^2\varphi\big)\end{aligned} \quad (3)$$

From Eqs. 2 and 3 we conclude that each manifold (including the $m_S = 0$ manifold) has its own, distinct quantization axis which, in general, is different from the direction of the applied magnetic field. In particular, the second term in Eq. 3 can be dominant for hyperfine couplings as low as 1 MHz (corresponding to nuclei beyond the first two shells around the NV) if ϑ is sufficiently large, implying that, in general, ^{13}C spins coupled to NVs misaligned with the external magnetic field experience a large frequency mismatch with bulk carbons, even if optical excitation makes $m_S = 0$ the preferred NV spin state.

Assuming fields in the range 10-30 mT, it follows that ^{13}C spins moderately coupled to the NV (300 kHz $\lesssim |A_{zz}| \lesssim$ 1 MHz) are dominant in the hyperpolarization process, not only because they are more numerous than those subject to strong couplings (i.e.,$|A_{zz}| \gtrsim$ 10 MHz corresponding to the first and second shells), but also because they more easily spin diffuse into the bulk (ultimately yielding the observable ^{13}C signal). For sweep rates near the optimum ($\sim$ 40 MHz/ms), the time necessary to traverse the set of transitions connecting $m_S = 0$ with either the $m_S = -1$ or $m_S = +1$ manifolds is relatively short $\big(\lesssim 30\ \mu$s for weakly coupled carbons$\big)$ meaning that optical repolarization of the NV preferentially takes place during the longer intervals separating two consecutive sweeps, as modeled in Fig. 3 of the main text.

The key to generating nuclear spin polarization is the selective non-adiabaticity of the mw sweep: Efficient polarization transfer takes place when the narrower Landau-Zener crossings connect branches with different electron and nuclear spin quantum numbers (Fig. 3 in the main text), precisely the case in the $m_S = 0 \leftrightarrow m_S = -1$ ($m_S = 0 \leftrightarrow m_S = +1$) subset of transitions when the hyperfine coupling is positive (negative). For moderately weak couplings ($|A_{zz}| \lesssim$1 MHz) the hyperfine interaction has a stronger 'dipolar-like' character (as opposed to 'contact-like' character) implying that positive and negative couplings balance out. Therefore, when probing ensembles, both sets of transitions behave in the same way, i.e., ^{13}C spins polarize positive in one direction, negative in the other (Fig. 4D in the main text).

Fig. S4A addresses the efficiency of the sweep mechanism in generating polarization as a function of the sweep velocity for two different hyperfine interactions and magnetic field alignments. For illustration purposes, we focus on the subset of transitions within the $m_S = 0 \leftrightarrow m_S = -1$ manifold and consider two cases where (i) the hyperfine interaction is $A_{zz} = A_{xx} = A_{yy} = 1$ MHz and $(\vartheta, \varphi) = (0°, 0°)$, and (ii) the hyperfine interaction is $A_{zz} = A_{xx} = A_{yy} =$ 500 kHz with $(\vartheta, \varphi) = (45°, 0°)$. In either case, we sample the system evolution over a 20 MHz window respectively centered at 2590 MHz and 2672 MHz, which we sweep either from lower to higher frequencies or, conversely, from higher to lower frequencies (upper and lower halves of the plot in fig. S4A).

In the above simulation we assume the initial NV spin state is $m_S = 0$ and consider ^{13}C spins completely unpolarized. At the end of the sweep, we calculate the expectation value $\langle I_{z'}\rangle$ of nuclear spins in the direction of the external magnetic field. The polarization is then shown as a function of the sweep velocity. For simplicity, we neglect throughout these calculations the effect of NV spin-lattice relaxation. NV spin repolarization events due to optical pumping can take place randomly during the sweep but the outcome remains virtually unchanged if most take place away from the Landau-Zener crossing. As a matter of fact, NV spin repolarization is indeed crucial for resetting the population back into the $m_S = 0$ subspace after the

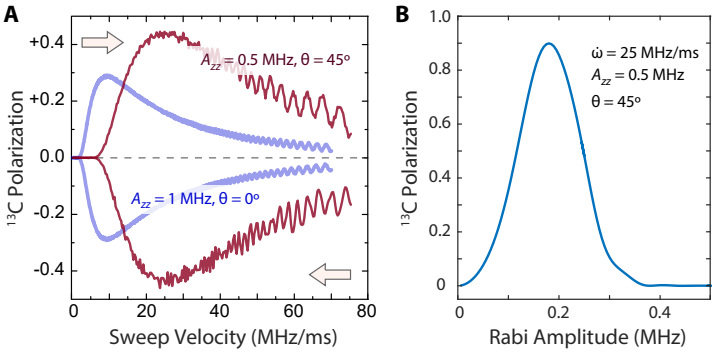

Figure S4. **Simulations of ^{13}C spin DNP enhancement.** (A) ^{13}C spin polarization as a function of the sweep rate for two different magnetic field orientations and hyperfine couplings. Arrows indicate the direction of the sweep; low-to-high (high-to-low) frequency sweeps yield positive (negative) nuclear spin polarization (upper and lower halves of the plot, respectively). (B) Polarization efficiency as a function of the Rabi field amplitude for the listed hyperfine coupling and magnetic field direction. In (A) and (B) we use $A_{zx} = 0.3A_{zz}$ and assume $A_{zz} = A_{xx} = A_{yy}$.

LZ passage, thus allowing for more polarization to be created in a second sweep. This argument holds for any subsequent sweeps and ultimately leads to a ratchet-like buildup of polarization that diffuses into the bulk.

Fig. S4B shows the calculated ^{13}C polarization as a function of the Rabi field amplitude for a single sweep assuming a hyperfine coupling $A_{zz} = A_{xx} = A_{yy} = 500$ kHz, a field direction $(\vartheta, \varphi) = (45°, 0°)$, and a sweep velocity $\dot{\omega} = 25$ MHz/ms. Consistent with the observations in Fig. 2D, we obtain an initial growth followed by a decay, with an optimum around 190 KHz. This response arises from the trade-off between the need to effectively drive the spin system throughout the full set of transitions and the widening gap between the two pairs of energy levels.

A complete simulation including all angular coordinates (ϑ, φ) and hyperfine interactions required to quantitatively compare the numerical results with our experiments is computationally-demanding and entails extensive additional work we will describe elsewhere.

IV. EXPERIMENTAL DESIGN

Our experimental setup consists of a fast field cycling device from 1mT-7T based on mechanical sample shuttling. The polarization transfer is performed at low field 1-30mT, after which the sample is rapidly shuttled to 7T for a high-sensitivity measurement of bulk ^{13}C polarization. While this was schematically represented in Fig. 1A of the main paper, here we describe the actual device construction (fig. S5). A more detailed analysis of the instrument will be presented elsewhere [40].

A. Construction and characteristics

The field cycler consists of a XY-tunable shuttling tower constructed over a 7T superconducting magnet with a low field magnetic shield positioned below it (see fig. S5). A conveyor belt driven actuator stage (Parker HMRB08) carries the sample along the fringing field of the magnet and into the shield. The sample is pressure-fit (fig. S5C) onto a carbon-fiber shuttling rod (8mm, Rockwest composites) that is fastened rigidly on a twin-carriage mount on the actuator stage (fig. S5A, B and G). The diamond powder is compactified by a plunger carrying a dielectric mirror (Thorlabs BB1-E02), which also serves to double pass the incoming laser radiation. The shuttler operates with a high positional precision of 50μm, over a 1600mm travel length, at a maximum speed of 2m/s and acceleration of 30m/s^2. The shuttling from 7T-8mT takes 648 ± 2.5ms with a remarkably high repeatability over months of operation. The shuttling is triggered by a pulse generator (SpinCore PulseBlaster USB 100 MHz) via a high voltage MOSFET switch (Williamette MHVSW-001V-036V) [40]. The end of the motion triggers the NMR instrument for inductive detection.

To minimize vibration and obtain optimal sample fill factors for detection, we align the carbon fiber rod parallel to the magnet to better than 1 mdeg over the entire distance of travel. Dynamic alignment is performed by two funnel-shaped guiding stages made of soft teflon at the magnet bore (fig. S5F), and the NMR probe. The NMR probe itself was designed hollow to accommodate fast sample shuttling to low fields below the magnet. ^{13}C detection at 75.03MHz was performed via printed saddle coils wrapped on a Quartz tube (9mm $\times$ 11mm Technical Glass Products).

B. Low field DNP volume

Polarization transfer from NV centers to ^{13}C nuclei is carried out at low fields (1-30mT) in a magnetically shielded volume (fig. S5E) below the 7T magnet. The shield is constructed by concentric layers of stress annealed iron (NETIC S3-6 alloy 0.062" thick, Magnetic Shield Corp.). Iron is used for its high magnetic saturation. The DNP field is tunable by varying position of the sample in the shield [**?**]. The shields are secured on sliding rails under the magnet (fig. S5E) to contain upward forces. Laser light is irradiated to the bottom of the test tube holding the sample (fig. S6). 200 mW of power provides 26.67 mW/mg to the diamond particles. Additionally, a MW antenna of 8.25 mm diameter applies swept-frequency microwave radiation that performs the polarization transfer (fig. S6B ,C).

V. DNP ELECTRONICS SETUP

Low field DNP is achieved by frequency sweeps over the NV center powder pattern during a continuous irradiation of laser light that polarizes the NV centers. Frequency sweeps are generated by a low-cost setup (fig. S7) involving voltage controlled oscillators (VCOs) – we use either Pasternack PE1V31012 (1.6-3.2 GHz) or Minicircuits ZX95-3800A+ (1.9-3.7 GHz). An inexpensive arbitrary waveform generator (Rigol 1022A) is AC coupled to a programmable power supply (Circuit Specialists) to provide the ramp inputs to the VCOs to carry out the frequency sweeps. We combine the AC and DC sources in a high-pass configuration with 3dB cutoff frequency $\approx$ 0.5Hz, and both sources are individually USB controlled allowing us to calibrate the exact sweep bandwidth to a target range. The VCO output amplitude $\approx$6dBm is controlled with a variable attenuator (Fairview SA1501SMA) to tune the MW Rabi frequency.

The microwave outputs from the VCOs are subsequently amplified with a 100W amplifier (Empower SKU1146) and delivered to the DNP excitation coil. Different NV centers effectively see a different Rabi frequency based on their orientation with respect to the coil axis, and those with their N-to-V axis approximately parallel to this axis do not contribute to hyperpolarization. In our experiments, we employ with similar results both loop (fig. S6B,) and saddle (fig. S6C) type coil geometries with the microwave fields $\mathbf{B}_{\mathrm{MW}}$ parallel and perpendicular to the bias field $\mathbf{B}_{\mathrm{pol}}$. In principle, a pill-box geometry that combines both orientations will provide a gain in hyperpolarization enhancement by about a factor of 2 (fig. S9).

In order to increase the polarization transfer efficiency, we use a

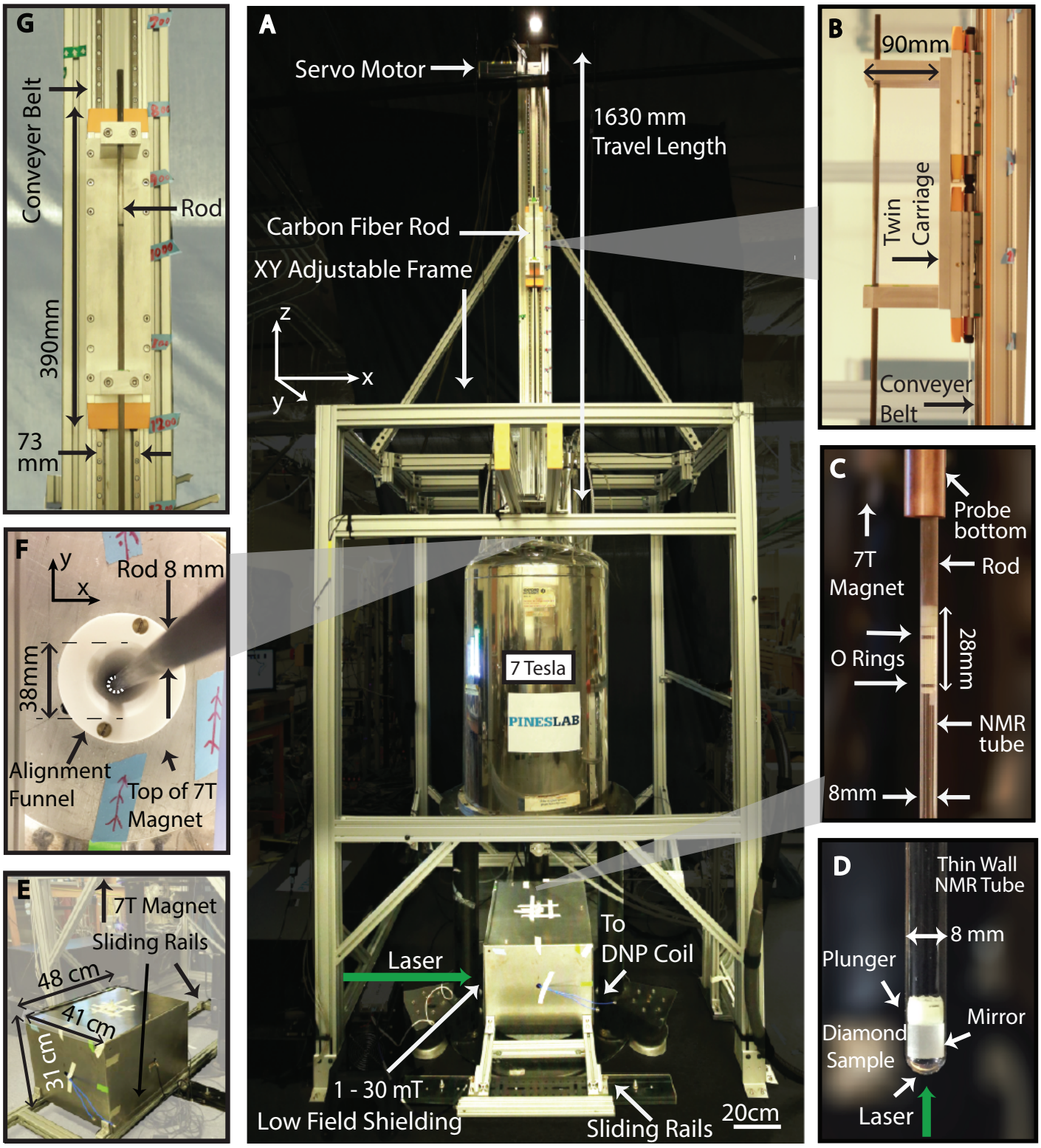

ht

Figure S5. Detail of experimental setup schematically described in Fig. 1A of main paper. (A) Mechanical shuttler constructed over a 7T superconducting magnet. Polarization transfer of ^{13}C in diamond particles is carried out by optical pumping at low field $\mathbf{B}_{pol}$ (1-30mT) in a shielded volume below the magnet (fig. S6), after which the sample is shuttled rapidly for measurement at 7T. A liquid nitrogen gun enables sample freezing at $\mathbf{B}_{pol}$. (B,G) Shuttling is enabled by a carbon fiber rod that carries the sample. The rod is mounted on a movable twin carriage on the fast conveyer belt actuator stage. (C) NMR tube that carries the sample is attached to the shuttling rod by a pressure fit arrangement using a pair of O-rings. (D) Diamond powder sample is contained with a dielectric mirror plunger employed to increase the efficiency of optical excitation. (E) Iron shield producing $\mathbf{B}_{pol}$ volume is placed on sliding rails to counter the magnetic force from the 7T magnet. (F) Bore of the 7T magnet is sealed with a teflon guide that ensures perfectly aligned shuttling and high fill-factor for inductive readout [40].

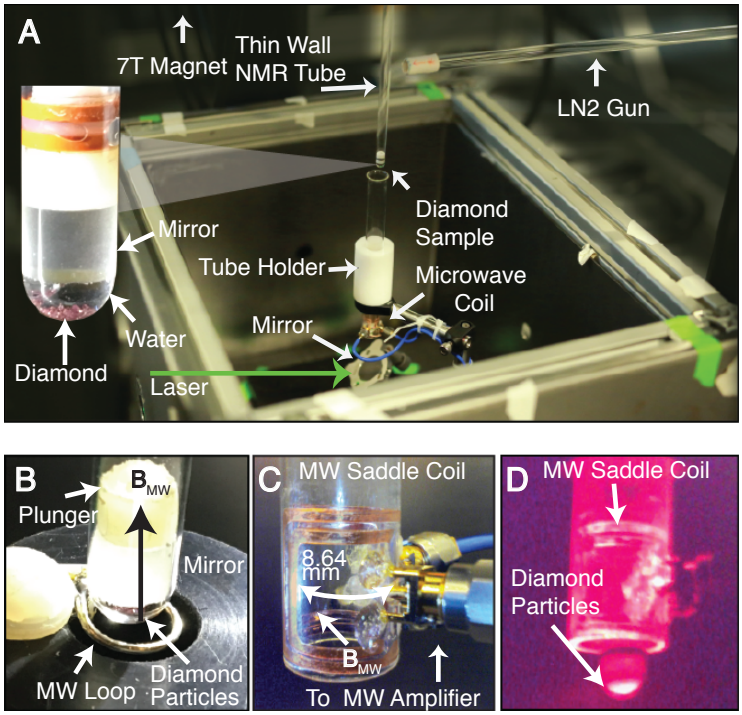

Figure S6. **Low field DNP setup.** Figure illustrates the setup for polarization transfer at low field ($\mathbf{B}_{\text{pol}} \sim$ 1-10 mT), performed inside a magnetic shield under the 7T NMR magnet. (A) The carbon fiber rod attached to the NMR tube carrying the diamond sample positioned inside the DNP excitation coil. Laser irradiation (5W over a 8 mm beam diameter) is applied from the bottom of the tube with a 45 degree mirror. *Inset:* Diamond particles immersed in water for better refractive index matching (fig. S1). We use for MW excitation either (B) stub-loop antennas or (C) printed saddle coils providing MW fields $\mathbf{B}_{\text{MW}}$ parallel or transverse to $\mathbf{B}_{\text{pol}}$. (D) Diamond particles under 1W laser illumination imaged with a 594nm long pass filter, showing the bright fluorescence from the NV centers.

novel technique of cascaded microwave sweeps created via multiple VCOs. While we shall present a detailed analysis of the technique in a forthcoming publication, we present here the basic principle and implementation. The method works by effectively increasing the total number of microwave sweeps in a given total pumping time by cascading the (N_{VCO}). For an optimal cascaded sweep, the output microwave frequencies are time-shifted by $2\pi/N_{\text{VCO}}$ to maximize the period between successive sweeps. The DNP enhancement gains can be made to scale linearly with N_{VCO} up to a certain limit set by the powder pattern (sweep bandwidth). With the simplicity of installing additional series of circuits, the addition of each VCO can be easily integrated into the design setup with the potential of additional sweepers allowing for large gains in polarization transfer efficiency.

The individual VCOs, even if of the same family, have slightly different frequency-voltage characteristics. To cascade the VCO sweeps effectively, we *match* their exact sweep bandwidths to within $\Delta f <$ 1MHz via a fast-feedback mechanism employing a spectrum analyzer (SignalHound SA44B) connected in parallel with the outputs (fig. S7). For matching, we employ a VCO sweep rate of 2kHz, allowing the output sweep spectrum to have a square-wave like shape, which is edge-detected in real time and feedback employed to converge to the target sweep bandwidth. The algorithm takes ≈2 min to converge, and allows one to leverage several MW sweepers simultaneously, enabling a simple means to boost polarization transfer efficiency.

VI. DNP OPTICS SETUP

Collimated 532 nm laser light (Coherent Verdi) is employed for the optical polarization of NV center electrons, which is then subsequently transferred to the ^{13}C nuclei by microwave irradiation. In practice, for the polarization of powders, the laser and swept microwaves are applied continuously (Fig. 1B of main paper). The laser power is controlled via a thin film polarizer and the half-wave plate (CVI TFP-532-PW-1025-C and QWPM-532-05-2, respectively) on a fine motorized rotation stage (Zaber RSW60A-T3). The laser beam is gated with an acousto-optic modulator (AOM, Isomet Corporation, M113-aQ80L-H), expanded to match the diameter of the NMR tube carrying the sample (8mm), and irradiated to the bottom of the tube. Fluorescence from the NV centers is imaged under a 594nm long pass filter (Semrock BLP01-594R-25) (fig. S5D).

For most DNP experiments we operated with a total laser power of ≈ 200mW over a 8mm beam diameter and 532nm excitation. We notice that the DNP efficiency decreases slightly at higher laser powers, which we attribute to the laser polarization breaking the coherence of the NV-^{13}C polarization transfer by repumping the NV center. Fig. S8 indicates that the optimal sweep rate employed for the microwave sweeps are independent of the laser power.

Let us now evaluate approximately the power employed per particle and per NV center. Assuming uniform distribution of laser power, each particle within the sample is hit with approximately 1mW. Using the total sample mass, the total number of particles, and the 1 ppm concentration of NV centers, it was determined that there are $1.31\pm0.13\times10^{12}$ NV centers per diamond particle. As a result, the laser power to NV center ratio per particle is $7.64\pm0.76\times10^{-13}$ mW/NV center. Overall this is a lower laser power than expected, and could indicate that the laser did not fully penetrate the diamond samples, thus reaching some NV centers and not others. Such a result would suggest potential for further enhancement if methods are developed to enhance laser penetration.

VII. SHOT TO SHOT VARIATION OF ENHANCEMENT

In our experiments, the DNP excitation coil producing the microwave sweeps is either transverse (saddle) or parallel (loop) to the 7T field. Moreover, when the particles are dry, they are free to reorient, and do so due to the jerk experienced during fast shuttling. This reorientation causes a shot-to-shot variation of the obtained enhancement (see fig. S9), since polarization cannot be transferred from NV centers that are parallel to the MW excitation. In future work, we plan to install a dual time-multiplexed MW excitation platform in both orthogonal directions parallel and transverse to the 7T field. This should allow a gain in average ^{13}C polarization by approximately a factor of 2 (fig. S9).

VIII. POLARIZATION LOSS DUE TO SHUTTLING

In our experiments, since the polarization transfer is performed in a different (low) field $\mathbf{B}_{\text{pol}}$ compared to where the ^{13}C polarization is detected, the measurement in fact underestimates the polarization created due to the losses during sample shuttling. Note that for our goal of optically hyperpolarizing a liquid via the polarized ^{13}C spins (Fig. 1C of main paper), we are concerned with the ^{13}C polarization at $\mathbf{B}_{\text{pol}}$, especially since the liquid ^{13}C T_1 is high at low fields.

In this section, we quantify the shuttling loss by measuring the T_1 of the ^{13}C spins as a function of position (field) and assuming a linear trajectory of motion. In total, the sample travels a distance

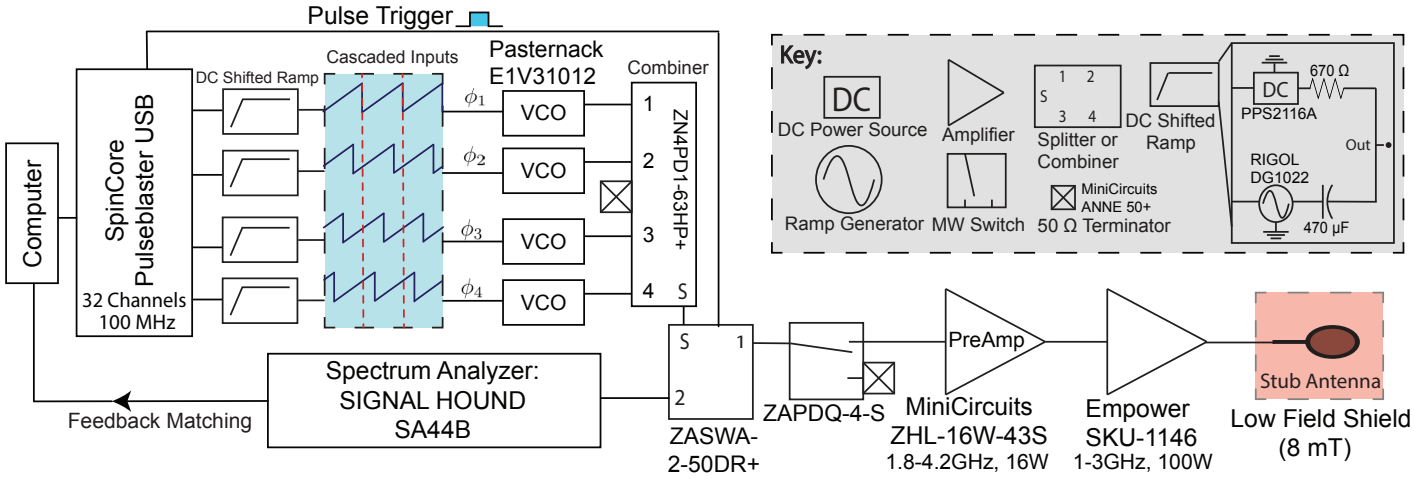

Figure S7. **Schematic circuit for DNP excitation.** Low field DNP from NV centers to ^{13}C is excited by microwave sweeps produced by employing voltage controlled oscillators (VCOs) with ramp generator inputs. Multiple VCOs are employed in a cascade to increase polarization transfer efficiency. A spectrum analyser is used to implement a feedback algorithm that exactly matches the VCO bandwidths to <2 MHz. The microwaves are finally amplified by a 100W amplifier into a stub antenna that produces either longitudinal or transverse fields (fig. S6) .

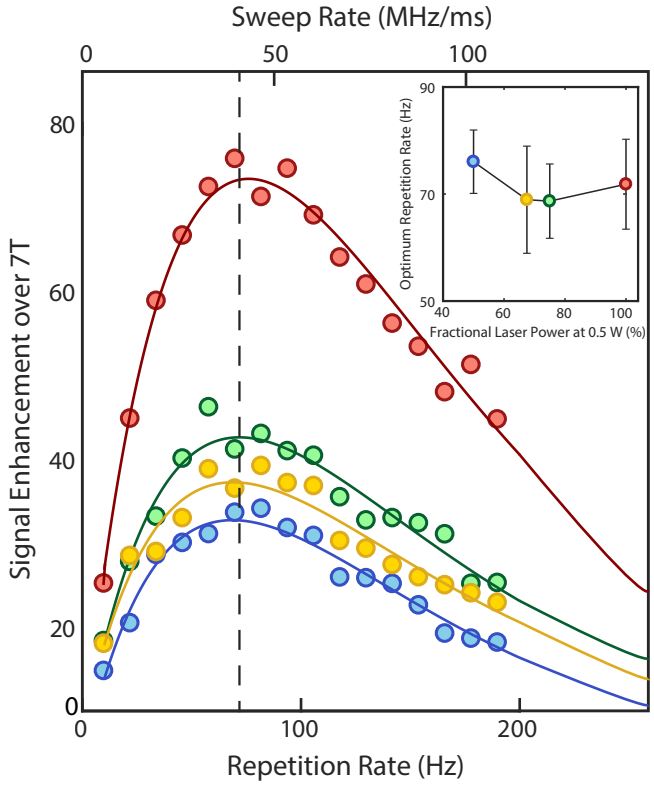

Figure S8. **Sweep rate dependence on laser power.** (Main) ^{13}C NMR signal as a function of the repetition (sweep) rate (lower and upper horizontal axes, respectively) for different illumination intensities. (Inset) The optimal repetition rate is nearly independent of laser intensity. In these experiments, the swept frequency bandwidth is 570 MHz and the laser beam diameter is 8 mm.

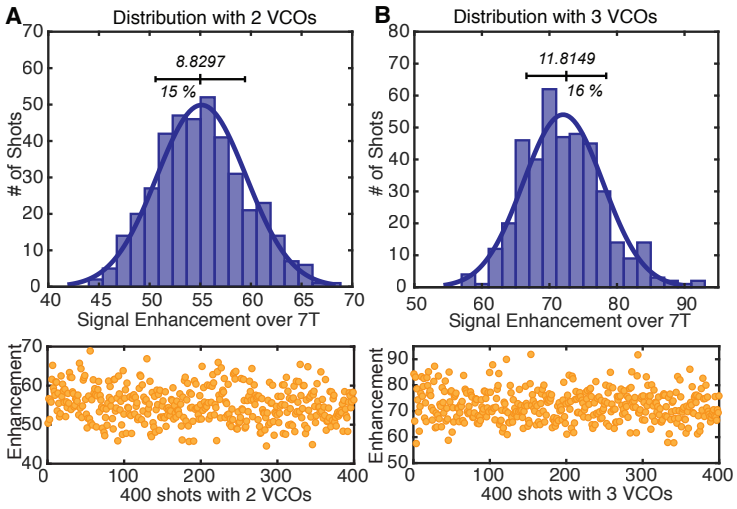

Figure S9. **DNP enhancement spread due to orientational shaking.** Panels illustrate the spread in the obtained DNP enhancement factor of the ^{13}C after 400 shots of the experiment measured at 7T for (A) 2 and (B) 3 VCOs sweeping the powder bandwidth. The mean spread is approximately 15% and we ascribe this to the orientational randomness of the powder for different experiment shots. It is also evident increasing the number of frequency sweepers leads to an enhanced DNP efficiency (fig. S7).

of $\Delta x = 829$mm to the NMR coil in $t_{\text{shuttle}} = 0.648$s. During this period, ^{13}C spins relax at a rate $R_z(B) = 1/T_1(B)$, where $T_1(B)$ is the field dependent spin relaxation constant. For the e6 diamond microparticles (Fig. 5C) these range from 10.19s (8mT) to 395.7s (7T), and correspond to decays between 6.66% and .176% respectively if static for t_{shuttle} at these fields. The exact amount of polarization loss can be quantified as,

$$\frac{dM_z(t)}{dt} = -R_z(M_z(t) - M_z^0) \tag{4}$$

where M_z^0 is the equilibrium magnetization. Integrating both sides, $\ln \frac{(M_z(t)-M_z^0)}{(M_z(0)-M_z^0)} = -\int_0^t \frac{1}{T_1(t)} dt$.

Using a numerical fit, we determine the equation of the experimentally obtained T_1 curve, $T_1(x) = 20.02423e^{.003893x}$, where x is the sample displacement from the low field position. Approximating the sample trajectory to be linear, we have $x(t) \approx \frac{829}{.648} t = 1279.3t$. Now solving Eq. (4), we estimate a polarization loss of only $\approx 1.03\%$ during shuttling. For samples with shorter low-field relaxation times, this polarization loss is greater, and our measurement provides a larger underestimate of the polarization at B_{pol}.

IX. DATA PROCESSING

In this section, we outline the procedure used for processing the ^{13}C NMR data, and evaluating the enhancement factor obtained via our low-field DNP protocol. Enhancement factor is calculated by comparing the ^{13}C signal at thermal equilibrium at 7T to our DNP signal. Because of the low inherent SNR, the thermal signal required 120 transients (N_{Thermal}) to obtain a clearly discernible signal.

For each data set, we appropriately phased and baseline-corrected each spectrum, and normalized the noise to unity. The enhancement was then calculated as the ratios of the normalized peak areas. To phase the spectra, we performed a zero-order phase correction that maximized the real portion of our peak by multiplying the real and imaginary portions of the peak by a phase value. The phasing algorithm detected both positive and negative peaks. Phased positive peaks had a reproducibly small range of phase values. Negative peaks, when phased to maximize the real portion of the peak, had phase values that were shifted by pi radians from the aforementioned range. By comparing measured phase values of a data set against the small range, the phasing algorithm detected whether the peak was positive or negative.

To correct the rolling baseline, we first used a peak detection algorithm. The peak detection algorithm fit an absorptive Lorentzian through the real portion of the peak, found the area of the entire fitted Lorentzian, and designated the signal limits such that the integral between the two limits was 90% of the total area. After we found the peak limits, and consequently the noise sections, we fit a 12th order polynomial through both noise sections and subtracted the polynomial from the phased peak. This resulted in a peak with a flat baseline.

Subsequently, to quantify signal enhancement, we scaled each spectrum such that the noise normalized to unity. This allows signals taken with different number of averages are put on the same footing, allowing a convenient way to characterize enhancement gains due to hyperpolarization. The noise was defined to be the standard deviation of the non-peak sections of the spectra. After scaling both spectra, we found the area under each peak (corresponding to their respective SNRs) by calculating the Riemann sum from the left peak limit to the right peak limit, and calculated the signal enhancement with respect to 7T thermal equilibrium as,

$$\varepsilon = \frac{\text{SNR}_{\text{DNP}}}{\text{SNR}_{\text{Thermal}}} \sqrt{\frac{N_{\text{DNP}}}{N_{\text{Thermal}}}} \tag{5}$$

At higher enhancements, the ratios of peak to noise are larger. Therefore phasing and baselining algorithms correct the peak heights proportionally to a greater extent compared to peaks of lower enhancement. This leads to the resulting curves being artificially non-smooth for certain data sets, which was not the case when the total absolute area was employed for each point. In order to account for this, we determined the ratio between the enhancement and the area for each data point, took the median of those ratios, and scaled the areas by the ratios to produce the final enhancement curves for all data sets.